Determining the Soil Water Characteristic Curve and Interfacial Contact Angle from Microstructural Analysis of X-ray CT Images

Kalehiwot Nega Manahiloh[1] and Christopher L. Meehan[2]

ABSTRACT

The complex behavior of unsaturated soils can be partly attributed to the co-existence of networks of liquid bridges and saturated pockets in the soil void space. Attempts have been made to understand the evolution of liquid bridges and pockets under changing suction in soils. The study described here utilizes one of these emergent technologies, X-ray micro Computed Tomography (X-ray micro-CT), to investigate unsaturated soil behavior. In this study, a partially saturated granular specimen is prepared and imaged under a controlled suction condition. Three dimensional images of interphase microstructure are acquired and processed using digital algorithms. The evolution of the liquid-gas and solid-liquid interfaces was tracked using 3D images obtained with phase-based segmentation. The Soil Water Characteristic Curve (SWCC) of the tested granular specimen was quantified by processing microstructural images that were obtained with X-ray CT scanning. Values of interfacial contact angle were measured on orthogonally projected planes and the associated results are presented and discussed.

Keywords: Soil water retention curve, Suction, Saturation, Contact angle, Unsaturated soil.

Citation Information: Please site this work as follows

Manahiloh Kalehiwot, N. and L. Meehan Christopher, *Determining the Soil Water Characteristic Curve and Interfacial Contact Angle from Microstructural Analysis of X-Ray CT Images.* Journal of Geotechnical and Geoenvironmental Engineering, 2017. **143**(8): p. 04017034.

Published version could be obtained from the following link

https://ascelibrary.org/doi/10.1061/%28ASCE%29GT.1943-5606.0001677

---

[1] Assistant Professor, University of Delaware, Dept. of Civil and Environmental Engineering, 301 DuPont Hall, Newark, DE 19716, U.S.A. E-mail: knega@udel.edu

[2] Bentley Systems Incorporated Chair of Civil Engineering & Associate Professor, University of Delaware, Dept. of Civil and Environmental Engineering, 301 DuPont Hall, Newark, DE 19716, U.S.A. E-mail: cmeehan@udel.edu

INTRODUCTION

The co-existence of networks of liquid bridges and saturated pockets in partially saturated soils yields complex soil behavior. Attempts have been made to understand the evolution of liquid bridges and pockets under changing suction conditions in soils

. However, historic limitations in the tools that have been available for microstructural observation have impeded the results of such efforts. Recent imaging advancements in the field of X-ray micro Computed Tomography (X-ray micro-CT) have allowed for pore-scale observation of multi-phase media, and have the potential to improve our understanding of the behavior of unsaturated soils (Higo et al., 2011, Manahiloh, 2013, Manahiloh and Muhunthan, 2012, Willson et al., 2012).

Previous research has shown that, among other parameters, relative permeability, degree of saturation, and capillary pressure have a dominant influence on multiphase flow in partially saturated media (e.g. Andrew et al., 2014). These macroscale parameters are in turn controlled by pore-scale topology, interfacial tension, and phase interaction at the interphase contacts (Chalbaud et al., 2009, Gaus, 2010, Plug and Bruining, 2007).

Proper understanding of the constitutive relationship between soil suction and saturation is of paramount importance for accurately modeling the engineering behavior of unsaturated soils (Lu and Likos, 2004, Manahiloh, 2013). A number of experimental setups and laboratory equipment have historically been used to determine the soil water characteristics curve (SWCC) of soils (Bocking and Fredlund, 1980, Cassel and Klute, 1986, Fredlund and Wong, 1989, Hilf, 1956, Houston et al., 1994, Phene CJ et al., 1971, Phene et al., 1971, Stannard, 1992). Saturation and/or drying is also inherently associated with the wettability behavior of the soil, which is governed by the contact angle made by the advancing or receding water-gas front (Andrew et al., 2014).

X-Ray CT allows visualization of the interior of objects by capturing digital information on their 3D microstructure (Denison et al., 1997, Masad et al., 1999). The image characterization results that are presented here were from tests performed at Washington State University (WSU) using a cone beam X-Ray FLASHCT (Flat Panel Amorphous Silicon High Resolution Computed Tomography) machine. The WSU facility houses an X-Tec 225 kV micro-focused X-Ray source for characterization at high magnification and a Pantak/Seifert 420 kV X-Ray source for component analyses requiring larger penetration (Fig. 1). The detector is a flat-panel Varian PaxScan 2520 with a CsI scintillator. Resolution close to 5 μm can be attained when scanning specimens with sizes on the order of a millimeter to a centimeter. The X-ray scanning system shown in Fig. 1 was designed to accommodate objects up to a diameter of 20 cm (8 in.) and a height of 46 cm (18 in.) so that special mounting apparatuses (such as triaxial cells) could be integrated into the test setup for load application during scanning. Software has been developed at WSU for system control, data acquisition, 3D imaging, and quantification of microstructural features. During scanning, intensity values are used to calculate the distribution of the linear attenuation coefficient, to generate cross-sections and 3D high-resolution digital images representing density at every voxel. (A voxel is a 1 x 1 x 1 element constituting a single gray value in an image; it is the 3D equivalent of a pixel). As will be shown later, brighter voxels correspond to higher-density objects such as soil grains, and dark voxels correspond to lower-density objects such as voids or pore fluid.

The centerpiece of this experimental study is an integrated X-ray micro-CT system that facilitates non-destructive microstructural characterization (Fig. 1). X-ray micro-CT is gaining popularity in material and geosciences studies. It has been utilized for a variety of applications, including: 3D pore characterization (Brunke et al., 2007, Manahiloh et al., 2012, Sakellariou et al.,

2010, Sok et al., 2010, Weinekoetter, 2008), 3D grain analysis (Ikeda et al., 2004, Jerram et al., 2009, Manahiloh and Muhunthan, 2012, Masad et al., 2005), fracture analysis (Bertels et al., 2001, Keller, 1998, Keller et al., 1999, Ketcham et al., 2010), multi-scale imaging (Manahiloh, 2013, Sok et al., 2010, Wildenschild and Sheppard, 2012), and fluid flow analysis (Chen et al., 2009, Dann et al., 2011, Manahiloh, 2013, Petchsingto and Karpyn, 2009, Wildenschild and Sheppard, 2012).

(a) (b)

Fig. 1. X-ray micro-CT system: (a) X-ray chamber, and (b) Associated X-ray sources.

In this work, a novel Tempe-cell type partially saturated specimen cell (Figs. 2a and 2c), developed by Manahiloh (Manahiloh, 2013), was used to control suction and saturation direction (i.e., wetting/drying) in a granular specimen housed inside an X-ray CT scanning chamber (Fig. 2) . Figures 2b and 2d show the general configuration of the X-ray CT system and the specimen to be scanned.

Subsequent sections describe the approach used to integrate microstructural image analysis with physical experiments. The associated image processing methodologies for quantifying the SWCC and contact angle of a partially saturated glass bead specimen are also presented; these methodologies have equal applicability to other studies involving granular geomaterials.

EXPERIMENTAL SETUP AND SPECIMEN PREPARATION

As noted, the emergence of X-ray micro-CT technology and its adoption in material science studies has enabled imaging of the internal microstructure of granular media. This non-destructive testing advancement allows for precise measurements that would not be otherwise achievable, which serve to further our understanding of the complex behavior of unsaturated soils. In particular, recent advancements in the attainable resolution allow for effective determination of the SWCC and measurement of interfacial contact angles.

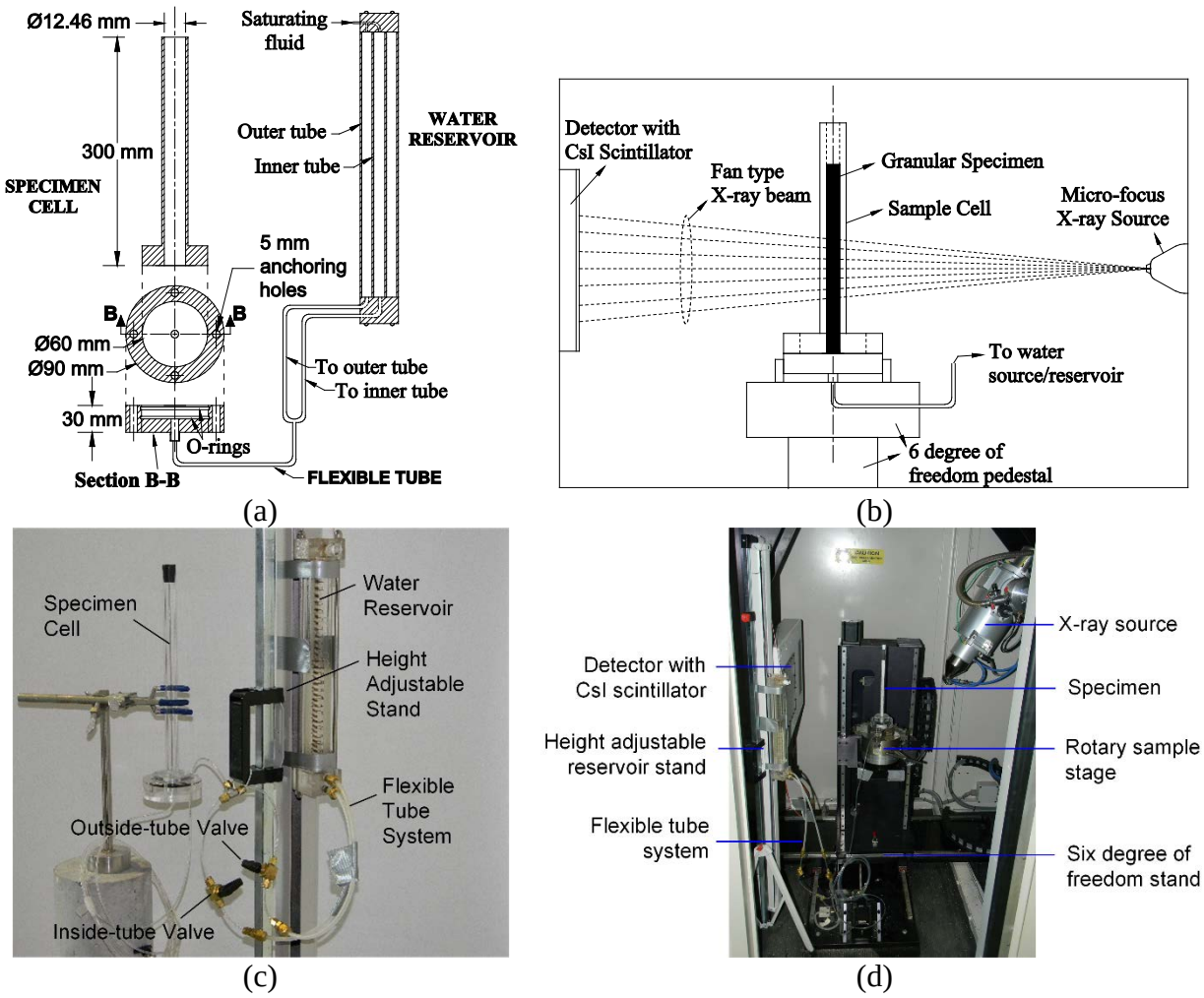

Fig. 2. (a) Schematic of specimen cell and saturation system, (b) Schematic of the general X-ray CT cabin and specimen configuration utilized in the current study, (c) Photo of experimental

setup at the specimen level, and (d) Photo of specimen cell mounted within the X-ray micro-CT system.

In order to assess the effectiveness of this technology for the desired application, the X-Tec 225 keV X-ray micro-CT source was used to scan a specimen composed of microsphere glass beads varying from 0.25 mm to 0.60 mm in diameter. The grain size distribution curve (C136-06, 2006) of the glass bead material that was used is shown in Fig. 3. The specific gravity of the glass beads was determined to be 2.50 (ASTM D854-14, 2014).

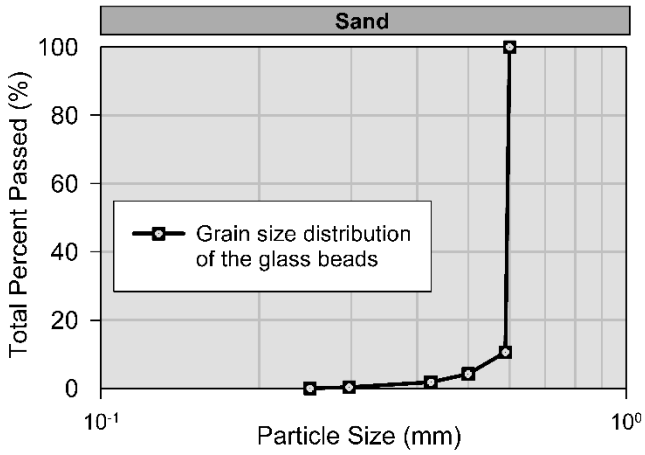

Fig. 3. Grain size distribution for the glass bead material.

An integrated system composed of an X-ray CT scanner, a specimen cell, 3-D image processing software, and integrated imaging algorithms was utilized for data collection and nondestructive characterization. Laboratory testing was carried out by saturating and drying a specimen inside a specially designed suction-controlled cell with concurrent X-ray CT imaging. The integrated sample cell and X-ray CT system used for the study are shown in Fig. 2d; a schematic of the imaging test setup is shown in Fig. 2b.

During the scanning process, the position of the sample relative to the detector and the X-ray source governs the spatial imaging resolution. In the experiments reported here, the distances

from the X-ray source to the sample and to the detector were measured to be 62 mm and 1048 mm respectively. This set up produced a corresponding spatial resolution of 30 μm.

To acquire a good resolution image, it is important to find out the correct combination of X-ray energy and current (flux) for each sample type and size. The correct energy ensures the X-rays are strong enough to penetrate through the thickest portion of the specimen and reach the detector. X-ray energy dictates the contrast between components of images. Too high energy results in low contrast images. The current (flux) refers to the number of photons per second per unit area. It is controlled by adjusting the electron beam flux (mA). Information on the scan energy and flux is given in Table 1. In the table, the first column contains information on the four stages that were used during the scanning process. In each stage, the specimen is equilibrated at different heads of water column to generate a range of suction data points. Detail about each stage and the associated suction-saturation data will be provided in subsequent sections.

Table 1. X-ray CT Scan Energy and Flux Data.

Stage	**Energy (keV)**	**Flux (μA)**
1	155	145
2	155	145
3	165	145
4	170	145

The glass bead specimen used in the current study was prepared by air pluviating ("raining") the beads directly from a funnel attached to the top of the specimen chamber; this yielded a specimen with an average initial void ratio of 0.40. The height of the compacted specimen, the inside diameter of the sample cell, and the total mass of the glass beads used were measured to be 225 mm, 12.46 mm, and 49 grams, respectively. The pore-fluid was distilled water lightly doped with CsCl (3% by weight), to increase the attenuation of X-rays and ensure better contrast of the liquid

phase from the air phase (Willson et al., 2012).

IMAGE ACQUISITION AND PROCESSING

Digital image processing consists of algorithms for contrast enhancement, noise reduction, image sharpening, segmentation, object recognition, and many other qualitative analyses (Razavi, 2006). Image processing has been used by a vast range of fields and its applications are increasing every day. Nowadays it plays a very important role in engineering, medicine, material sciences, agricultural, and other natural science studies. Recently, the application of digital image processing to geotechnical engineering is gaining popularity. In geotechnical engineering, digital images may be processed to study the flow (Yu), deformation (Higo et al., 2013), and strength (Oda et al., 2004) related behaviors of geomaterials. For X-ray CT testing, digital image analysis can also be used to find the numbers, dimensions, and orientations of soil particles, investigate the distribution of pores, quantify porosity and anisotropy, and perform a variety of other microstructure-related analyses.

X-ray CT image acquisition was performed over 360 degrees to create a high-resolution three-dimensional tomographic dataset. This feature makes the cone beam X-ray CT scanner many times faster than other conventional linear detector array systems. In the linear detector array systems, a fan of ray is emitted from the X-ray source. The images acquired with such beams will be single X-sectional area images. For complete scan, user needs to move the sample up or down following each image acquisition. In the cone-type-beam however, the rays capture volumetric information and the sample need not be moved, thus saving imaging acquisition time.

A set of interactive software programs was used to control the data acquisition, image construction, and specimen visualization. To further refine or filter images to extract desired specimen properties and other information of interest, the collected images must be post-

processed. During each test, scanning of samples was initiated using an application-specific Flat Panel Amorphous Silicon High-resolution Computed Tomography (FlashCT) data acquisition system (DAQ). This program controls the hardware operation, calibration and image acquisition (HYTEC, 2004). Using this DAQ, the datasets are saved as unified directory structure (UDS) files, which are text files containing data fields separated by linefeeds that can be later processed by the Data Processing System software (FlashCT DPS) to perform image construction. In the FlashCT DPS software package, the UDS header files are reconstructed into two dimensional image slices. Calibration files are then utilized to correct pixel-to-pixel differences in the detector (i.e., to perform "bad pixel" correction). These calibration files contain radiographs taken with no object in the field of view. They range from completely dark images, when an image is taken with no radiation exposure, to light fields when an image is taken with full exposure (HYTEC, 2004).

Physical centering the axis of rotation at the middle of the cropped region of the detector while aligning the system is one of the most challenging steps in the scanning process. A one pixel offset of an image may result in a 50% loss of resolution (HYTEC, 2004). Since perfect centering of the sample is difficult to attain, post-centering correction algorithms are employed to reconstruct an image with corrected slope and intercept (where, slope quantifies the deviation of sample's vertical edges from the true vertical and intercept refers to the difference between the sample center and the axis of rotation of the sample pedestal). These algorithms analyze image sinograms and correct the system's center of rotation with respect to the entered data to yield reconstructions of the images with the centering problem rectified. Fig. 4 shows an example image of a porous concrete specimen before and after centering correction.

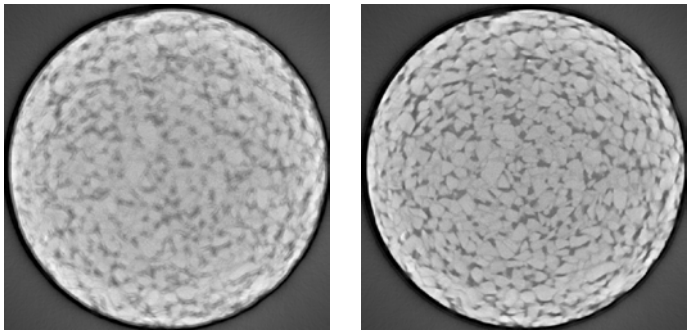

(a) **(b)**

Fig. 4. Example porous concrete X-ray CT images showing the effect of proper centering correction: (a) uncorrected image, and (b) corrected image.

Reconstruction of three-dimensional images from a series of two-dimensional slices is performed as the last phase before the images are transferred to other post-image-processing software programs such as Matlab® (MathWorks, 2004) and Image-Pro Plus® (Media Cybernetics, 2004). The software platform associated with the Washington State University (WSU) X-ray CT system is FlashCT Visualizing (VIZ). A summary of the overall processes involved with X-ray CT scanning is shown in Fig. 5.

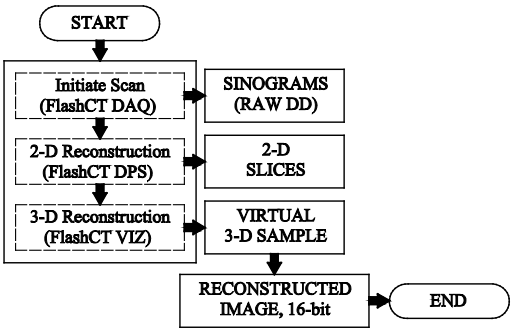

Fig. 5. General flow of the X-ray CT scanning process.

A digital image is a representation of a discrete function with an integral (gray scale) or rational (Red, Green, Blue) number ranges. The fundamental constituent element of a digital image is a pixel (1x1 square) in 2-D and a voxel (1x1x1 cube) in 3-D as shown in Fig. 6. The intensity of

an image at a point is represented by the value of each pixel or voxel.

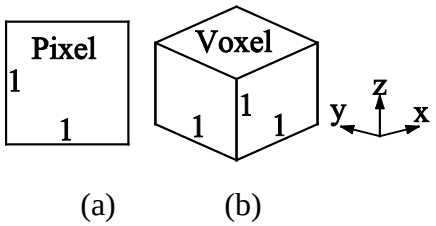

Fig. 6. Idealization of: (a) a pixel, and (b) a voxel.

Computational resources play a significant role in digital image processing. Good performance typically requires the use of relatively fast parallel processing (i.e., 3.0 GHz / processor) with 4 hyper-threaded processors, and 4GB of RAM per core. The computational system utilized at WSU meets these requirements, and consequently prevents memory-related shortcomings that can be encountered in the image pre-processing stages. In the data acquisition process, the data corresponding to voxel gray shades are stored as 16-bit integers ranging between 0 and 65,535. For image post-processing, the unsigned 16-bit data demands relatively large amounts of memory.

To circumvent memory problems, the data was converted to 8-bit integers ranging from 0 to 255. For the glass bead images, this conversion showed negligible effects on image resolution but significantly reduced image size to a level that allowed relatively fast processing.

IMAGE SEGMENTATION

When numerical evaluation or quantification of features in images is performed, all images undergo a step called segmentation. In segmentation, the major aim is to split the image domain into distinct regions. The segmentation criteria used in this study targets intra-region uniformity, a criterion dictating regions to be uniform and homogenous, and inter-region disparity, a criterion dictating that adjacent regions should have a significant contrast. Most unsupervised segmentation methods use a combination of both inter-region and intra-region metrics. A typical example of a

global segmentation approach that uses these combinations is Otsu's segmentation technique (Otsu, 1979).

Otsu's method tries to find a threshold value which minimizes the within-class variances (i.e. intra-region) of background and foreground voxel classes, which is equivalent to maximizing the variance between the means of the two clustered classes (i.e. inter-region) (Gebrenegus, 2009, Sund and Eilertsen, 2003, Wirjadi, 2007). In Otsu's thresholding technique, for an image taking on discrete voxel values *k*, the optimal threshold, θ, is given as:

$$\theta_{Otsu} = \arg\max_{\theta} \left\{ \sum_{k<\theta} p(k)(\mu_0 - \mu)^2 + \sum_{k\geq\theta} p(k)(\mu_1 - \mu)^2 \right\} \tag{1}$$

Where: $p = \text{Normalized histogram}$; $\mu = \text{Mean}\{f(x)\}$; $\mu_1 = \text{Mean}\{f(x) \mid f(x) \geq \theta\}$; and $\mu_0 = \text{Mean}\{f(x) \mid f(x) < \theta\}$

Otsu's segmentation gives accurate results if there are no local inhomogeneities. Unfortunately, such inhomogeneities exist in the majority of geomaterials of interest and the application of Otsu's segmentation technique can return many misclassified voxels in a given segmented image. Even with extreme optimization of the acquisition parameters for better quality reconstructions, there is always "noise" when global thresholding techniques are applied for segmentation.

A solution to such instances is to use local adaptive thresholding techniques. These are region-based approaches that take into account the information in the direct neighborhood of each point of the domain. One example of a local adaptive segmentation technique is that of Li (Li et al., 2008). Because Li's approach uses an iterative minimization technique, an initial solution has to be provided to the method; to start with a good initial guess, initialization is usually performed using the results from Otsu's segmentation.

The general process of segmentation followed in this study can be illustrated using a single X-ray CT slice (Fig. 7). The 8-bit raw X-ray CT slice obtained from a partially saturated glass-bead specimen (Fig. 7a) is investigated using a segmentation approach and the gray values of pixels belonging to each phase are determined. These gray values can then be input into the image processing software program and the program can be instructed to render each phase in a different color. The result of this step is shown as Fig. 7b, where the overall grayscale ranges shown in Fig 7a are "binned" to three distinct black, gray and white colors that signify the gas, liquid and solid phases, respectively. Using masking techniques, individual phase of interest can be segmented by masking others. The results from this technique, as applied to extracting the solid, liquid, and gas phases from Fig. 7b, are shown in Figs. 7c, 7d and 7e, respectively. For this specific image, the ranges of gray values for the gas, liquid and solid phases were (0 – 30), (31 – 120), and (121 – 255), respectively. Any information sought on each phase can then be stored in arrays, with stored information later being used to calculate various engineering parameters. Example parameters that were calculated in this work include degree of saturation and interface angle.

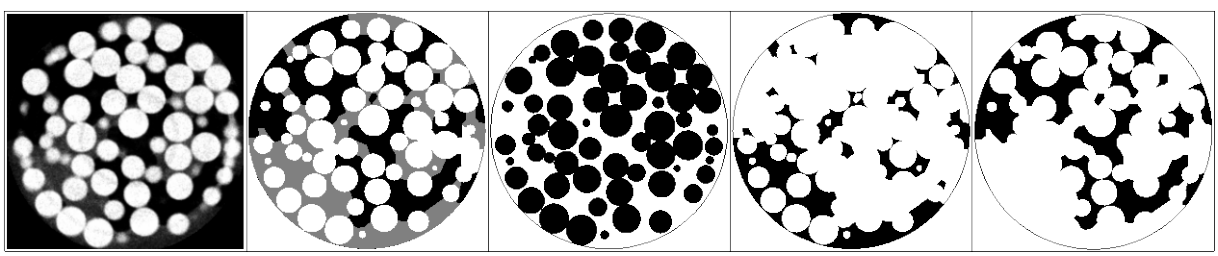

(a) (b) (c) (d) (e)

Fig. 7. Image segmentation: (a) raw image; (b) three-phase segmented image; (c) Image segmented for solid phase only; (d) Image segmented for liquid phase only; (e) Image segmented for gas phase only.

SOIL WATER CHARACTERISTIC CURVE FROM MICROSTRUCTURAL IMAGE ANALYSIS

The SWCC provides a conceptual understanding between the mass (and/or volume) of pore-water and the energy state of the water phase (Fredlund et al., 2012, Pham, 2005). It also provides a

constitutive framework for combining the theory of unsaturated soil behavior and unsaturated soil properties, and plays a pivotal role in the solution of unsaturated soil problems (Fredlund et al., 2012). Common laboratory techniques used to apply matric suction and measure the equilibrium water content include tensiometers (Cassel and Klute, 1986, Stannard, 1992), axis translation techniques (Bocking and Fredlund, 1980, Hilf, 1956), electrical/thermal conductivity sensors (Fredlund and Wong, 1989, Phene CJ et al., 1971, Phene et al., 1971), and contact filter paper methods (Houston et al., 1994). In this paper a new approach for determining the SWCC is presented, in which the degree of saturation is obtained from digital image processing by means of thresholding and automated voxel-counting. Using this approach, the liquid and gas phase volumes in the specimen were determined using image-processing macros which counted voxels in the digital imagery (Media Cybernetics Manufacturing, 2003). The resulting degree of saturation values were expressed as percentages by taking the ratios of the voxel counts corresponding to the liquid phase, V_L, and void (gas plus liquid) phase, V_V. To illustrate this process, consider the image shown in Fig. 7. For a uniform thickness slice, the volume ratio that is used in defining the degree of saturation (Equation 2) could be rewritten using the area ratio shown in Equation 3. The area of the phases of interest, in turn, is equal to the number of dots (pixels) that make up the area. Therefore, from the images, the area is calculated as the total number of pixels that have gray values within a defined range.

$$S = \frac{V_W}{V_v} \times 100\% \tag{2}$$

$$S = \frac{A_W}{A_v} \times 100\% = \frac{A_{liquid}}{A_{gas} + A_{liquid}} \times 100\% \tag{3}$$

For the defined area of interest shown in Fig. 7, the following pixel counts were obtained.

- Gas: 9157
- Liquid: 8849

- Solid: 24806

Using Equation 3,

$$S = \frac{A_{liquid}}{A_{gas} + A_{liquid}} \times 100\% = \frac{8849}{9157 + 8849} \times 100\% = \mathbf{49.17}\%$$

A partially saturated specimen was scanned in four stages, two along a drying path and two along a wetting path of the SWCC. This was to ensure that X-ray CT images of the granular and fluid microstructure were obtained over a sufficiently large enough range to infer the remainder of the SWCC. Matric suction was applied to the specimen by integrating a cellulose membrane at the base of the sample cell (Figs. 2a and 2c) and applying suction using a hanging column system (ASTM D6836-02, 2008). For each of the test stages, the reference datum was fixed and the location of water inside the specimen was carefully marked and used in calibrating the variation of suction inside the cell. A small opening was provided at the top of the sample cell to ensure the air pressure was atmospheric, as shown in Fig. 2c.

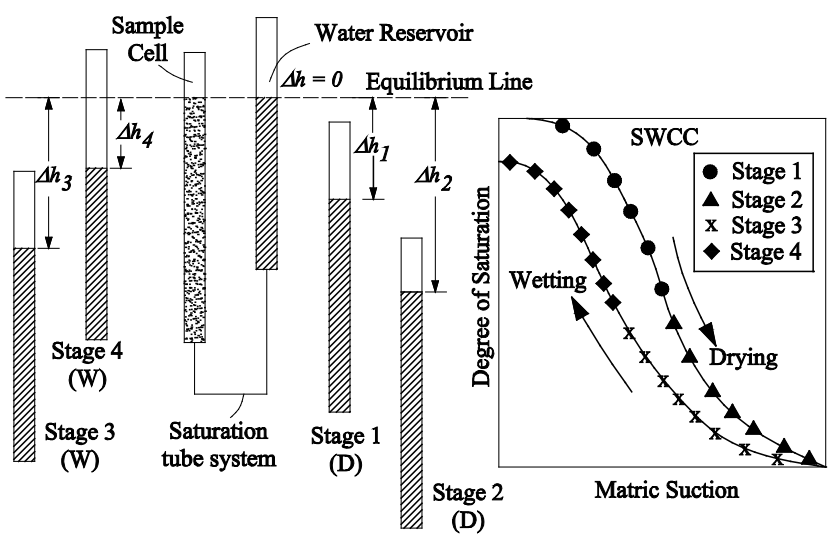

Fig. 8. Schematic showing the experimentally controlled suction and wetting process.

Figure 8 provides a schematic of the water reservoir conditions under which the four scanning stages were implemented. Stage 1 represents the initiation of drying of the specimen from

its fully saturated condition. In this stage, the suction head (Δh_1) was set to 7 cm. Details regarding the scanned and suction measurement locations for Stage 1 are shown schematically in Fig. 9. The locations indicated within the specimen were all in reference to the base of the specimen column. In Stage 2 the water reservoir in the hanging column was lowered to cause a total head difference (Δh_2) of 21.5 cm and further dry the sample column. Stage 3 represents initiation of re-wetting of the specimen. This was achieved by raising the water reservoir such that the head difference at equilibrium (Δh_3) was reduced to 12 cm. Finally, in Stage 4, the suction head (Δh_4) was further reduced to 4 cm to continue the wetting path.

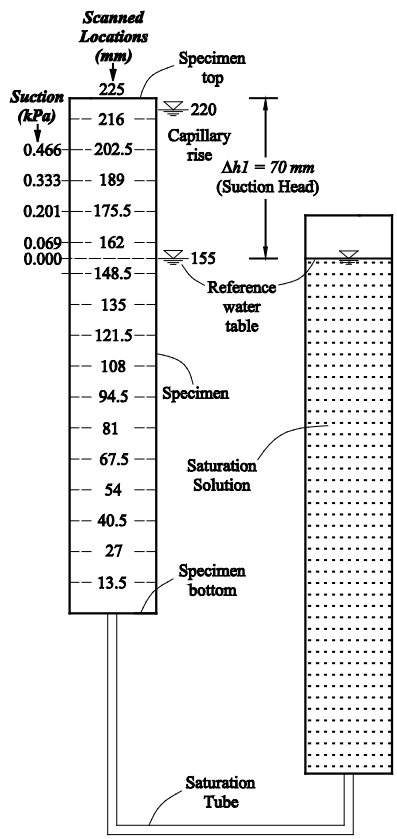

Fig. 9. Scanned locations and measured suction values for Stage 1.

Data for the measured suction and calculated saturation are presented in Table 2. To obtain the numerical values for the degree of saturation that are shown in Table 2, an image processing

macro was developed and implemented.

Table 2. Data on Measured Suction and Calculated Degree of Saturation.

Stages	Measurement Location (mm)	Suction (kPa)	Saturation (%)
Stage 1 (Drying)	155.0	0.000	97.34
	162.0	0.069	97.18
	175.5	0.201	97.04
	189.0	0.333	95.70
	202.5	0.466	85.50
Stage 2 (Drying)	70.0	0.588	66.75
	80.0	0.686	44.94
	90.0	0.784	35.17
	100.0	0.882	31.79
	130.0	1.176	21.24
	160.0	1.471	18.67
	190.0	1.765	6.74
	220.0	2.059	3.80
Stage 3 (Wetting)	220.0	1.127	1.28
	190.0	0.833	7.63
	165.0	0.588	12.42
	135.0	0.294	60.04
Stage 4 (Wetting)	220.0	0.343	38.40
	215.0	0.294	53.81
	205.0	0.196	82.21
	200.0	0.147	84.30
	195.0	0.098	86.40
	185.0	0.000	86.40

Since Gardner's 1958 work (Gardner, 1958), a number of empirical equations have been suggested to best fit the SWCC data obtained from laboratory experiments (Brooks and Corey, 1964, Fredlund and Xing, 1994, McKee and Bumb, 1984, Pham and Fredlund, 2006, van Genuchten, 1980). In this work, the experimental data collected for the SWRC from the integrated X-ray apparatus was fitted with Van Genuchten's 1980 model (1980), as shown in Fig. 10. Using the Van Genuchten model fit approach (for which the equation is provided in Fig. 10), S_s and S_r represent the saturated and residual saturations respectively, ψ is the matric suction, α is a

parameter related to the inverse of the air-entry suction, and *n* is a non-dimensional measure of the pore-size distribution. Relatively large *n* values are indicative of uniform pore size distribution. *m* is another fitting parameter that takes role in controlling the symmetry of the SWCC. This parameter controls the slope of the characteristic curve in the relatively high suction range, where relatively small *m* values result in a steeper slope at higher suctions.

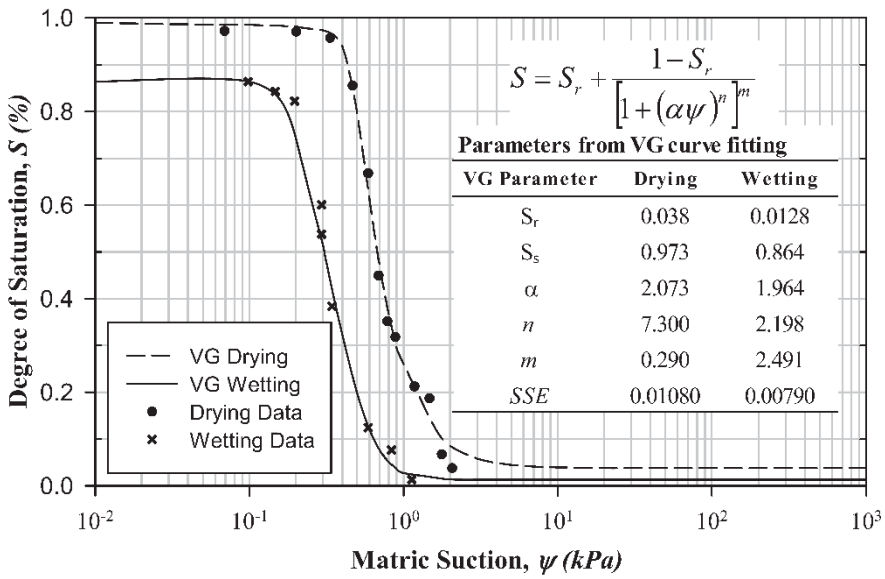

Fig. 10. Van Genuchten (VG) fit Soil water retention curve for the glass bead material.

INTERFACIAL CONTACT ANGLE FROM MICROSTRUCTURAL IMAGE ANALYSIS

The interfacial contact angle has been defined as the angle measured from the liquid-solid interface to the liquid-gas interface (Jury and Horton, 2004), and it is believed to be an intrinsic property of any two contacting phases in a solid-liquid-gas system (Lu and Likos, 2004). For unsaturated soil systems, the contact angle has been defined as the angle between a line tangent to the gas-water interface and a line defined by the liquid-solid interface. This definition is shown in Fig. 11. Generally speaking, contact angle is a widely used measure of wettability of surfaces (Anderson, 1986).

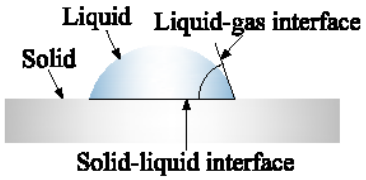

Fig. 11. Definition of contact angle**.**

When a soil pore fluid (e.g., water) is preferentially attracted to the solid phase compared to its cohesive attraction to other liquid molecules, the contact angle is small and the liquid is said to "wet" the solid. Conversely, when the cohesive force of the liquid is much stronger than the attractive force to the solid, the liquid is said to "repel" the solid (Jury and Horton, 2004). In many liquid-solid-gas interfaces, the wetting solid-liquid contact angle is substantially larger than the drying contact angle. In a capillary tube filled with water, a wetting contact angle will lead to capillary rise. On the other hand, a similar capillary tube filled with mercury will exhibit a repellant contact angle, which leads to capillary depression (Lu and Likos, 2004).

There are a number of contact angle measurement techniques. Some commonly utilized approaches are the dynamic sessile drop method (Dickson et al., 2006, Espinoza and Santamarina, 2010), the captive bubble method (Chiquet et al., 2007), and methods that use micro-model studies (Chalbaud et al., 2009). Although such measuring techniques are accurate, their utility is limited to cases where the solid is a flat surface. In cases where the solid and/or the solid-liquid interface occurs in a nonplanar or curved form, the reproducibility of the above techniques becomes questionable. For soil mechanics applications, nonplanar interfacial surfaces dominate the solid-liquid interactions in the majority of naturally occurring geomaterials, including unsaturated granular soil. Consequently, there is a need for other direct contact angle quantification techniques that account for this non-planarity.

There is limited work that has been performed that uses digital image processing to

measure contact angle. Most existing work makes use of classic angle measuring techniques. Some studies have used goniometers in the sessile drop and/or the modified sessile drop methods (e.g. Dickson et al., 2006, Espinoza and Santamarina, 2010). A few studies have tested the applicability of X-ray micro tomography for contact angle measurement (e.g. Andrew et al., 2014). However, those studies did not account for phase curvature and surface roughness. Very recently, a study by Andrew *et al.*(Andrew et al., 2014) used X-ray micro tomography on CO_2-brine-carbonate to investigate contact angle. To date, no study has utilized X-ray micro-CT and digital image processing to investigate the evolution of the interfacial boundary while simultaneously measuring the associated contact angle in a partially saturated granular media.

This paper presents the results from a series of X-ray micro-CT imaging tests conducted under a suction controlled environment on a partially saturated granular specimen comprised of a glass bead material. From the X-ray CT images, the three distinct phases (solid, liquid, and gas) can be clearly delineated using a range of X-ray attenuation coefficients to define each phase. As shown in Fig. 12a, pixel coloring is correlated to X-ray attenuation, with the lightest colored pixels corresponding to the solid phase, the darkest colored pixels corresponding to the gas phase, and the intermediate (gray) pixels corresponding to the water phase.

For the X-ray CT equipment that was used in the current study, the base color level for each imaging scan is not constant; this means that a different pixel color range needs to be used to define the respective solid, liquid, and gas phases for each imaging scan. This phenomenon of varying base color can be clearly observed in Fig. 12b, which shows a series of sequential scans that were performed along the length of the column. The whole length of the specimen was scanned in small segments to achieve good resolution of the three phases. The difference in the brightness of each segment can be attributed to the consistency in energy and flux emission as a function of

the length of time the X-ray scanner was in continuous use. Visual differences in brightness do not negatively affect image analysis, provided each segment is analyzed independently and pixel color ranges are assigned accordingly, as was done in the current study.

In order to measure contact angle values directly within a given specimen, it is necessary to focus on the characteristics of a localized feature; this type of close analysis requires the use of high-definition X-ray CT images. In general, the scale at which a given feature must be assessed is a function of the solid particle sizes that are in contact and the resulting void space between the particles. For the current study, the relative size of a typical feature of interest is shown in Fig. 12a.

The following section shows how the results from digital image processing can be used to measure individual interfacial contact angles for a given feature. The presented contact angle-measurement approach is shown to be particularly beneficial, in that it can be applied to curved interfaces, not just the traditional flat interfaces that are utilized with glass plate testing approaches.

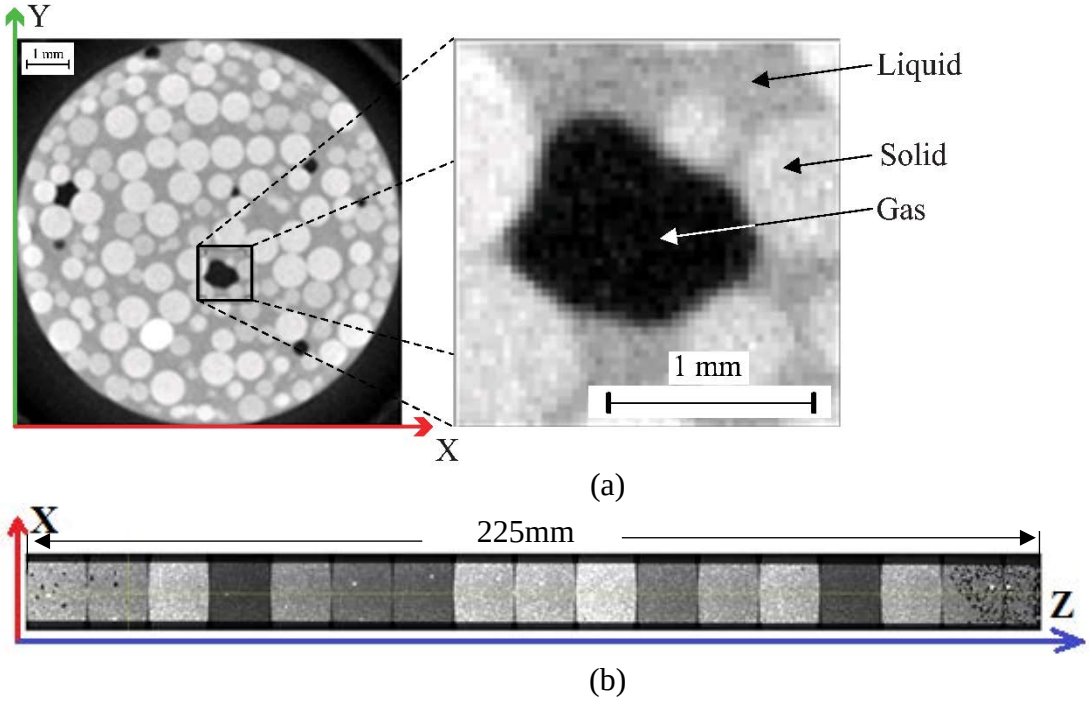

Fig. 12. (a) An example X-Y image "slice" from the analyzed specimen (left) and a sub volume

for which an analysis ganglion was defined (right), and (b) Sequential images along the height (X-Z) of the analyzed specimen.

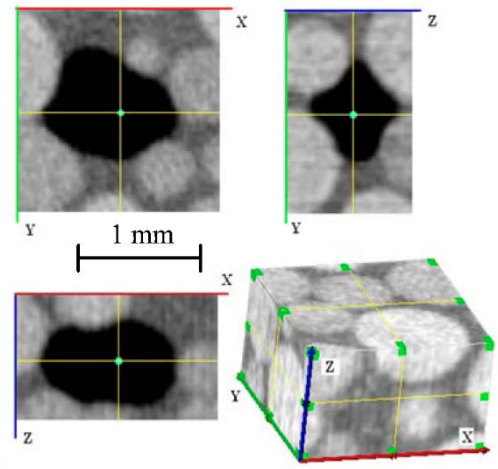

Fig. 13. Typical Coordinate Axes system.

Figure 13 shows a cubic image sample that contains an included air-ganglion feature of interest that can be used for interphase angle assessment; the image set shown corresponds to the sample location identified in Fig. 12a. Figure 13 also shows the coordinate axis system that was used. For this cubic sample, the evolution of the interfacial contact surface across three orthogonal planes is shown in Figs. 14 through 16. The image slices in Fig. 14 show the spatial variation of the contact surface over one full air ganglion in the *z*-direction (i.e. the "main direction" of fluid saturation/desaturation in the soil column). In a similar fashion, the images in Figs. 15 and 16 show the spatial variation of the contact surface in the *y*- and the *x*-directions across the air-ganglion, respectively.

In order to generate the images shown in Figs. 14 through 16, noise was removed by applying 3 passes of a 3 by 3 kernel-sized median filter. With this type of image enhancement filter, the impulse noises are removed by replacing each center pixel with the median value of its neighborhood pixels. The range of histogram was also adjusted to further filter out gray values

associated with impulse noise that were left out by the median filter. In addition, all edges were enhanced by applying a single pass of a 3 x 3 Laplacian filter, to improve the identification of the inter-phase boundaries.

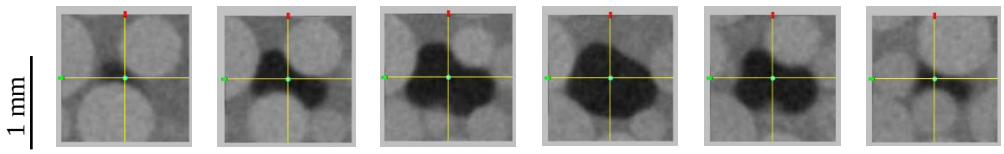

z = 8 *z* = 12 *z* = 16 *z* = 20 *z* = 24 *z* = 28

Fig. 14. Cross-sectional images taken in the *z*-direction, [image centered at (x, y) = (22, 22)].

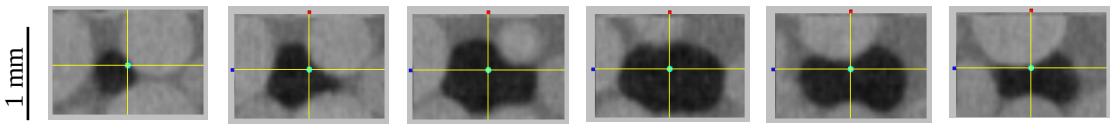

y = 12 *y* = 16 *y* = 20 *y* = 24 *y* = 28 *y* = 32

Fig. 15. Cross-sectional images taken in the *y*-direction, [image centered at (x, z) = (22, 16)].

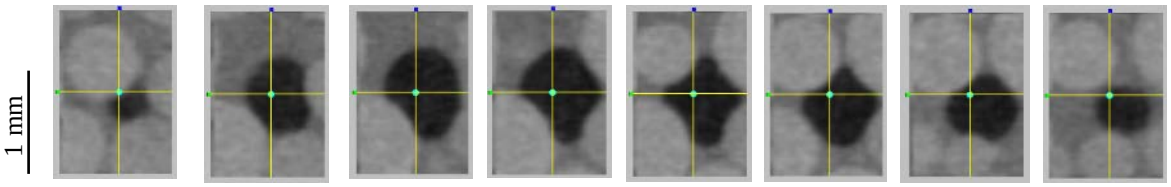

x = 8 *x* = 12 *x* = 16 *x* = 20 *x* = 24 *x* = 28 *x* = 32 *x* = 36

Fig. 16. Cross-sectional images taken in the *x*-direction, [image centered at (y, z) = (22, 16)].

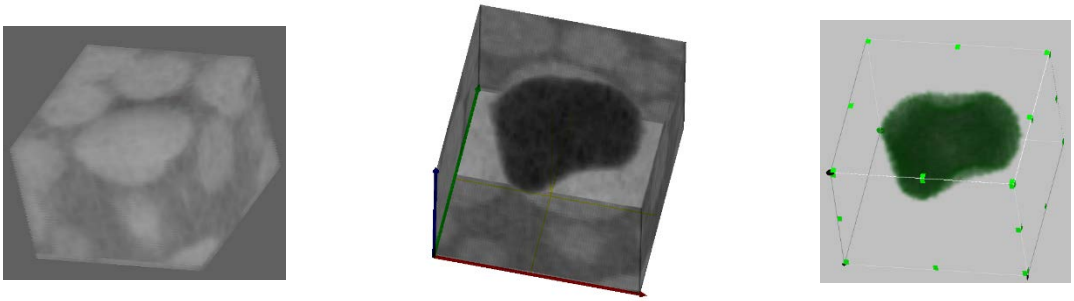

(a) (b) (c)

Fig. 17. (a) Three dimensional volume resulting from the reconstruction of the 2-D slices shown in Figures 14 through 16, (b) & (c) 3-D renderings showing the air-ganglion bounded by the liquid and solid phases.

A total of 20 images are shown in Figs. 14 through 16, each of which possess a number of interface contact angles around the edge of the air ganglion (Figs. 17b and 17c). From these images, three orthogonal planes were chosen to measure the angles formed between the solid-liquid and liquid-gas interfaces (i.e. contact angle) for the tested specimen (Media Cybernetics). The measured angles of interest for the three planes of characterization are provided in Figs. 18 through 20, along with the corresponding feature locations for each measured angle.

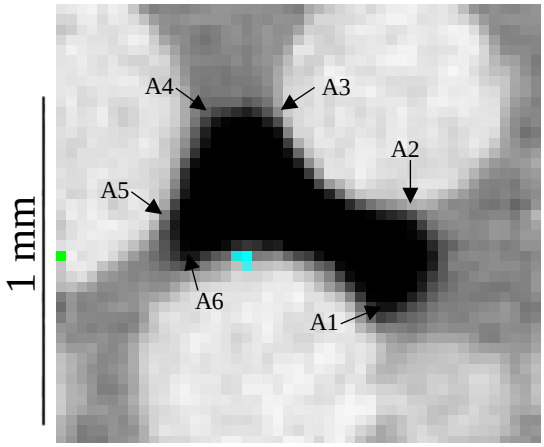

Angle	Value (°)
A1	87.9
A2	88.1
A3	88.1
A4	87.7
A5	88.2
A6	89.4
Avg.	**88.3**
STDEV	**0.64**

Fig. 18. Measurements on the XY plane located at Z = 11.

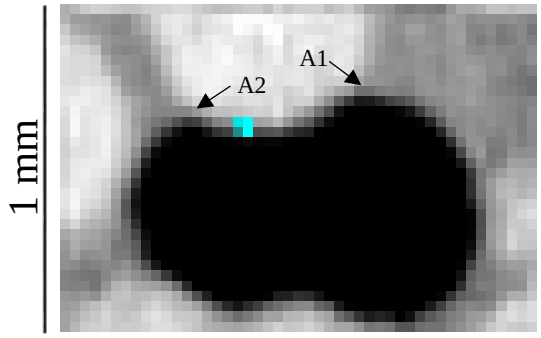

Angle	Value (°)
A1	88.8
A2	89.3
Avg.	**88.75**
STDEV	**0.78**

Fig. 19. Measurements on the XZ plane located at X = 26.

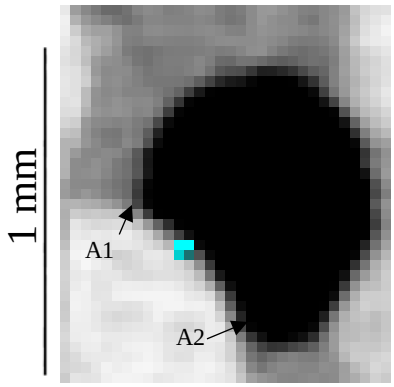

Angle	Value (°)
A1	87.9
A2	88.3
Avg.	**88.1**
STDEV	**0.28**

Fig. 20. Measurements on the YZ plane located at Y = 17.

For the three images that were analyzed, the average contact angle values for the XY, XZ, and YZ planes were found to be 88.3°, 88.75°, and 88.1°, respectively. The standard deviations (STDEV) were found to be 0.64, 0.78, and 0.28, respectively. The number of measurements taken from each image varied depending on the presence of actual contact between liquid and solid phases. The relatively larger values of contact angle that were observed in this study suggest that the glass bead material is mildly hydrophobic. Performing contact angle measurements on the same material, but flat in this case, resulted in a contact angle of 87.3° when there is no fluid movement, and wetting and drying contact angles of 123.2° and 36.7° when the flat plane was inclined at 30°. Figs. 21a and b show the images taken for contact angle measurement on a flat material. It is interesting to observe that the curvature of the beads did not significantly change the measured contact angles. Under flow equilibrium conditions, the average angles measured for flat (87.3°) and spherical (88.4°) materials differ by only 1°.

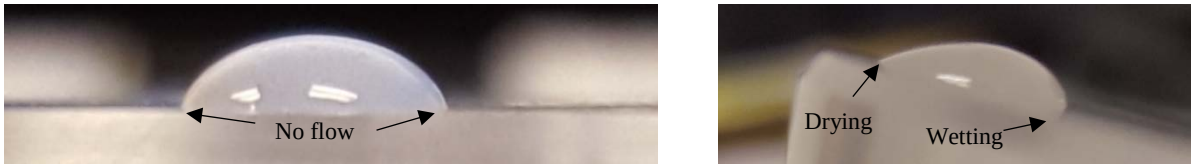

(a) (b)

Fig. 21. A droplet prepared from a 3% CsCl doped water solution: (a) No flow, and (b) Plane tilted by 30° to initiate flow to the right.

CONCLUSIONS

A physical experimental approach integrated with digital image processing was shown to be useful for quantifying parameters of fundamental importance in unsaturated soil mechanics. A direct method that enabled identification of interfacial boundary surfaces, quantification of the SWCC, and the contact angle between the solid-liquid and the liquid-gas interfaces was presented. Theoretically, the presented technique has no application limitations and could be used in cases involving surface curvature and roughness, i.e. for any unsaturated studies dealing with granular geomaterials. The only necessary criterion is obtaining high resolution microstructural images, for which the potential applicability of X-ray micro-CT scanners was demonstrated. An image processing algorithm was developed and used for quantifying the degree of saturation of a partially saturated granular specimen in an automated manner. The use of a 3% by weight CsCl solution enabled separating the liquid phase from the gas phase that co-existed in the pore spaces. The average interfacial contact angles measured on the XY, XZ, and YZ planes were found to be 88.3, 88.75, and 88.1 degrees, respectively. The overall average contact angle measured for the partially saturated glass bead material was 88.4 degrees. It was observed that the curvature didn't significantly alter the magnitude of the measured interfacial contact angle. In general, the tested glass bead assembly exhibited a hydrophobic behavior, which is consistent with what was observed in the flat glass plate tests.

REFERENCES

Anderson, W. G. (1986). "Wettability Literature Survey- Part 2: Wettability Measurement." *Journal of Petroleum Technology*, 38(11), 1246-1262.

Andrew, M., Bijeljic, B., and Blunt, M. J. (2014). "Pore-scale contact angle measurements at reservoir conditions using X-ray microtomography." *Advances in Water Resources*, 68, 24-31.

ASTM D854-14 (2014). "Standard Test Methods for Specific Gravity of Soil Solids by Water Pycnometer." *ASTM International*West Conshohocken, PA, .

ASTM D6836-02 (2008). "Standard Test Methods for Determination of the Soil Water Chararcteristic Curve for Desorption Using a Hanging Column, Pressure Extractor, Chilled Mirror Hygrometer, and/or Centrifuge." ASTM International, West Conshohocken, PA.

Bertels, S. P., DiCarlo, D. A., and Blunt, M. J. (2001). "Measurement of aperture distribution, capillary pressure, relative permeability, and in situ saturation in a rock fracture using computed tomography scanning." *Water Resources Research*, 37(3), 649-662.

Bocking, K. A., and Fredlund, D. G. "Limitations of the axis translation technique." *Proc., The 4th International Conference on Expansive Soils*, 117-135.

Brooks, R. H., and Corey, A. T. (1964). "Hydraulic properties of porous media." *Colorado State University Hydrology paper, No. 3. Fort Collins, CO.*

Brunke, O., Neuber, D., and Lehmann, D. K. "NanoCT: Visualizing of internal 3D-structures with submicrometer resolution." 325-331.

C136-06, A. (2006). "Standard test method for sieve analysis of fine and coarse aggregates." *ASTM International*West Conshohocken, PA.

Cassel, D. K., and Klute, A. "Water potential: tensiometry." *Proc., Klute, A. (Ed): Methods of Soil Analysis: Part 1. Physical and Mineralogical Methods* American Society of Agronomy -Soil Science Society of America, 563-596.

Chalbaud, C., Robin, M., Lombard, J. M., Martin, F., Egermann, P., and Bertin, H. (2009). "Interfacial tension measurements and wettability evaluation for geological CO2 storage." *Advances in Water Resources*, 32(1), 98-109.

Chen, C., Packman, A. I., and Gaillard, J. F. (2009). "Using X-ray micro-tomography and pore-

scale modeling to quantify sediment mixing and fluid flow in a developing streambed." *Geophysical Research Letters*, 36(8), L08403.

Chiquet, P., Broseta, D., and Thibeau, S. (2007). "Wettability alteration of caprock minerals by carbon dioxide." *Geofluids*, 7(2), 112-122.

Dann, R., Turner, M., Close, M., and Knackstedt, M. (2011). "Multi-scale characterisation of coastal sand aquifer media for contaminant transport using X-ray computed tomography." *Environmental Earth Sciences*, 63(5), 1125-1137.

Denison, C., Carlson, W. D., and Ketcham, R. A. (1997). "Three-Dimensional Quantitative Textural Analysis of Metamorphic Rocks Using High-Resolution Computed X-Ray Tomography: Part I. Methods and Techniques." *Journal of Metamorphic Geology*, 15, 29-44.

Dickson, J. L., Gupta, G., Horozov, T. S., Binks, B. P., and Johnston, K. P. (2006). "Wetting phenomena at the CO 2/water/glass interface." *Langmuir*, 22(5), 2161-2170.

Espinoza, D. N., and Santamarina, J. C. (2010). "Water-CO2-mineral systems: Interfacial tension, contact angle, and diffusion—Implications to CO2 geological storage." *Water Resources Research*, 46(7), W07537.

Fredlund, D. G., Rahardjo, H., and Fredlund, M. D. (2012). *Unsaturated Soil Mechanics in Engineering Practice*, Wiley & Sons, Inc., Hoboken, New Jersey.

Fredlund, D. G., and Wong, D. K. H. (1989). "Calibration of thermal conductivity sensors for measuring soil suction." *Geotechnical Testing Journal*, 12(3), 188-194.

Fredlund, D. G., and Xing, A. (1994). "Equations for the soil-water characteristic curve." *Canadian Geotechnical Journal*, 31(3), 521-532.

Gardner, W. R. (1958). "Some steady steat solutions of the unsaturated moisture flow equation with application to evaporation from a water-table." *Soil Science Journal*, 85(4), 228-232.

Gaus, I. (2010). "Role and impact of CO2–rock interactions during CO2 storage." *International Journal of Greenhouse Gas Control*, 4, 73-89.

Gebrenegus, T. (2009). "Application of X-ray Computed Tomography to Study Initiation and Evolution of Surface Cracks in Sand-Bentonite Mixtures." PhD, University of Idaho, Moscow.

Higo, Y., Oka, F., Kimoto, S., Sanagawa, T., and Matsushima, Y. (2011). "Study of strain localization and microstructural changes in partially saturated sand during triaxial tests using microfocus x-ray ct." *Soils and Foundations*, 51(1), 95-111.

Higo, Y., Oka, F., Kimoto, S., Sanagawa, T., Sawada, M., Sato, T., and Matsushima, Y. (2013). "Visualization of Strain Localization and Microstructures in Soils during Deformation Using Microfocus X-Ray CT." *Advances in Computed Tomography for Geomaterials*, John Wiley & Sons, Inc., 43-51.

Hilf, J. W. (1956). "An investigation of pore water pressure in compacted cohesive soils." *Technical Memorandum No. 654*, United States Department of the Interior, Bureau of Reclamation, Design and Construction Division, Denver, CO.

Houston, S. L., Houston, W. N., and Wagner, A. (1994). "Laboratory filter paper suction measurements." *Geotechnical Testing Journal*, 17(2), 185-194.

HYTEC (2004). *FlashCT Software User Manual*, HYTEC INC., Los Alamos, NM.

Ikeda, S., Nakano, T., Tsuchiyama, A., Uesugi, K., Suzuki, Y., Nakamura, K., Nakashima, Y., and Yoshida, H. (2004). "Nondestructive three-dimensional element-concentration mapping of a Cs-doped partially molten granite by X-ray computed tomography using synchrotron radiation." *American Mineralogist*, 89(8-9), 1304-1313.

Jerram, D. A., Mock, A., Davis, G. R., Field, M., and Brown, R. J. (2009). "3D crystal size distributions: A case study on quantifying olivine populations in kimberlites." *Lithos*, 112, 223-

235.

Jury, W. A., and Horton, R. (2004). *Soil Physics, Sixth Edition*, Wiley, Hoboken, New Jersey.

Keller, A. (1998). "High resolution, non-destructive measurement and characterization of fracture apertures." *International Journal of Rock Mechanics and Mining Sciences*, 35(8), 1037-1050.

Keller, A. A., Roberts, P. V., and Blunt, M. J. (1999). "Effect of fracture aperture variations on the dispersion of contaminants." *Water Resources Research*, 35(1), 55-63.

Ketcham, R. A., Slottke, D. T., and Sharp Jr, J. M. (2010). "Three-dimensional measurement of fractures in heterogeneous materials using high-resolution X-ray computed tomography." *Geosphere*, 6(5), 499-514.

Li, C., Kao, C. Y., Gore, J. C., and Ding, Z. (2008). "Minimization of region-scalable fitting energy for image segmentation." *Image Processing, IEEE Transactions on*, 17(10), 1940-1949.

Lu, N., and Likos, W. J. (2004). *Unsaturated Soil Mechanics*, Wiley, Hoboken, New Jersey.

Manahiloh, K. N. (2013). "Microstructural Analysis Of Unsaturated Granular Soils Using X-Ray Computed Tomography." PhD Dissertation, Washington State University.

Manahiloh, K. N., and Muhunthan, B. (2012). "Characterizing Liquid Phase Fabric of Unsaturated Specimens from X-Ray Computed Tomography Images." *Unsaturated Soils: Research and Applications*, C. Mancuso, C. Jommi, and F. D'Onza, eds., Springer Berlin Heidelberg, 71-80.

Manahiloh, K. N., Muhunthan, B., Kayhanian, M., and Gebremariam, S. Y. (2012). "X-Ray Computed Tomography and Nondestructive Evaluation of Clogging in Porous Concrete Field Samples." *Journal of Materials in Civil Engineering*, 24(8), 1103-1109.

Masad, E., Muhunthan, B., Shashidhar, N., and Harman, T. (1999). "Internal Structure Characterization of Asphalt Concrete Using Image Analysis." *ASCE, Journal of Computing in Civil Engineering*, 13(2), 88-95.

Masad, E., Saadeh, S., Al-Rousan, T., Garboczi, E., and Little, D. (2005). "Computations of particle surface characteristics using optical and X-ray CT images." *Computational Materials Science*, 34(4), 406-424.

MathWorks (2004). "Image Processing Toolbox User's Guide: Version 5." The MathWorks Inc., Natick, MA.

McKee, C. R., and Bumb, A. C. (1984). "The importance of unsaturated flow parameters in designing a hazardous waste site." *Hazardous Waste and Environmental Emergencies: Hazardous Materials Control Research Institute National Conference* Houston, TX, 50-58.

Media Cybernetics "ImagePro-Plus." Media Cybernetics, Inc. Silver Spring, MD, USA.

Media Cybernetics (2004). "Image-Pro Plus Version 5.0. for Windows: Auto-Pro Reference." *MAN AP 7846N00 20040229*, Media Cybernetics, Silver Spring, MD.

Media Cybernetics Manufacturing (2003). "Image-Pro(P) Plus with 3D Constructor." Media Cybernetics, Inc.

Oda, M., Takemura, T., and Takahashi, M. (2004). "Microstructure in shear band observed by microfocus X-ray computed tomography." *Géotechnique*, 54(8), 539-542.

Otsu, N. (1979). "Threshold Selection Method from Gray-Level Histograms." *IEEE Trans. Syst., Man Cybernetics*, SMC-9(1), 62-66.

Petchsingto, T., and Karpyn, Z. T. (2009). "Deterministic modeling of fluid flow through a CT-scanned fracture using computational fluid dynamics." *Energy Sources, Part A: Recovery, Utilization and Environmental Effects*, 31(11), 897-905.

Pham, H. Q. (2005). "A Volume-mass constitutive model for unsaturated soils." PhD PhD Thesis, University of Saskatchewan, Saskatoon, SK.

Pham, H. Q., and Fredlund, D. G. "A volume-mass constitutive model for unsaturated soils." *Proc.*,

Fifty-Eighth Canadian Geotechnical Conference, 173-181.

Phene CJ, Hoffman GJ, and SL., R. "Measuring soil matric potential in-situ by sensing heat dissipation within a porous body: I. Theory and sensor construction." *Proc., Soil Science Society of America* 225-229.

Phene, C. J., Hoffman, G. J., and Rawlins, S. L. "Measuring soil matric potential in-situ by sensing heat dissipation within a porous body: I. Theory and sensor construction." *Proc., Soil Science Society of America* 27-33.

Plug, W. J., and Bruining, J. (2007). " Capillary pressure for the sand–CO2–water system under various pressure conditions. Application to CO2 sequestration." *Adv Water Rresour*, 30, 2339-2353.

Razavi, M. R. (2006). "Experimental and numerical investigation of shear localization in granular material." PhD Dissertation, Washington State University, Pullman.

Sakellariou, A., Kingston, A. M., Varslot, T. K., Sheppard, A. P., Latham, S. J., Sok, R. M., Arns, C. H., Senden, T. J., and Knackstedt, M. A. "Tomographic image analysis and processing to simulate micro-petrophysical experiments." *Proc., Developments in X-ray Tomography Vii*, The Australian National Univ.

Sok, R. M., Varslot, T., Ghous, A., Latham, S., Sheppard, A. P., and Knackstedt, M. A. (2010). "Pore scale characterization of carbonates at multiple scales: Integration of micro-CT, BSEM, and FIBSEM." *Petrophysics*, 51(6), 379-387.

Stannard, D. I. (1992). "Tensiometers- Theory, Construction, and Use." *Geotechnical Testing Journal*, 15(1), 48-58.

Sund, R., and Eilertsen, K. (2003). "An algorithm for fast adaptive image binarization with applications in radiotherapy imaging " *IEEE Transactions on Medical Imaging*, 22, 22-28.

van Genuchten, M. T. (1980). "A closed-form equation for predicting the hydraulic conductivity of unsaturated soils." *Soil Sci. Soc. Am. J*, 44(5), 892-898.

Weinekoetter, C. "X-ray nanofocus CT: Visualising of internal 3D-structures with submicrometer resolution." 3-14.

Wildenschild, D., and Sheppard, A. P. (2012). "X-ray imaging and analysis techniques for quantifying pore-scale structure and processes in subsurface porous medium systems." *Advances in Water Resources*, 51, 217-246.

Willson, C. S., Lu, N., and Likos, W. J. (2012). "Quantification of grain, pore, and fluid microstructure of unsaturated sand from X-ray computed tomography images." *Geotechnical Testing Journal*, 35(6), 911-923.

Wirjadi, O. (2007). "Survey of 3D Image Segmentation Methods." *Fraunhofer ITWM*, Kaiserslautern, Germany.

Yu, M. "Effect of persulfate formulations on soil permeability." M.Sc., Washington State University.